Formation of Size-Selected Ni/NiO Core−Shell Particles by Pulsed Laser Ablation

Kaname Sakiyama,[†] **Kenji Koga,**[‡] **Takafumi Seto,***[,†] **Makoto Hirasawa,**[†] **and Takaaki Orii**[†]

Research Consortium for Synthetic Nano-Function Materials Project (SYNAF), National Institute of Advanced Industrial Science and Technology (AIST), Central 2, 1-1-1 Umezono, Tsukuba, Ibaraki 305-8568, Japan

This paper presents the method for fabricating size-selected nickel nanoparticles (diameter: 5−20 nm) coated with nickel oxide shells (thickness: about 2 nm). The core−shell particles were synthesized by a series of sequential gas-phase processes including pulsed laser ablation, aerosol postannealing, size-classification, compulsory oxidation, and aerosol-jet deposition. The change in the size distribution of the generated particles due to postannealing was measured by a low-pressure differential mobility analyzer (LP-DMA) coupled with a Faraday cup electrometer. The peak size decreased as the postannealing temperature rose, indicating that a sintering and restructuring of the agglomerates was taking place. In the high-resolution TEM (HRTEM) observation, the Ni particles of less than 15 nm in diameter were found to be spherical and single crystal after the annealing at 1073 K. The 20 nm particles were also spherical, but they remained polycrystalline due to insufficient annealing treatment required for recrystallization. The change in the surface morphology due to the compulsory oxidation was analyzed by the HRTEM and electron diffraction. Finally, monodispersed (geometric standard deviation < 1.2) Ni/NiO core−shell particles with oxidized surface layers of 2 nm and particle diameters ranging from 5 to 20 nm were successfully fabricated.

Introduction

Studies on nanometer-sized particles (nanoparticles) have progressed rapidly over the past decade. Nanoparticles have properties distinct from those of bulk materials, and their potentials for application are attracting attention.[1,2] In view of the considerable influences of size, surface, and morphology on the properties of nanoparticles, it will be crucial to develop technologies to fabricate well-controlled particles. Among the various types of nanosized particle, those fabricated from a transition metal and below a certain critical size have superparamagnetism,[3] a unique property derived from the fluctuation of magnetization due to thermal energy. Superparamagnetism has made it difficult to apply nanoparticles to the next generations of ultrahigh-density recording media. One way to surmount this problem would be to fabricate monodispersed and isolated nanoparticles from a material with large magnetic anisotropy. On the basis of this concept, Sun et al.[4] developed a liquid-phase synthesis technique to fabricate FePt nanocrystal superlattices. Extensive investigations have focused on the fabrication of magnetic nanoparticle arrays made from Co[5] and Fe_3O_4.[6] These liquid-phase techniques normally require a postannealing process to reduce impurities, to crystallize the nanoparticles, and to obtain the nanoparticle arrays. However, it is very difficult to separately control crystallization, surface structure, and agglomeration, three factors that significantly influence the properties of nanoparticles. Moreover, these "batch" and "wet" processes allow impurities to infiltrate the system at significant levels; hence, they are considered unsuit-

able for sequential and clean processes such as those used in semiconductor manufacturing.

On the other hand, gas-phase synthesis processes such as evaporation−condensation,[7] chemical vapor condensation,[8] flame synthesis,[9] arc discharge,[10] and sputtering[11] are considered clean and sequential processes, as the nanoparticles can be produced in the high-purity carrier gas stream. The challenge with these processes lies in the control of the particle morphology, which can be disrupted by the random collision of gas atoms. Pulsed laser ablation (PLA)[12] is a super clean system that employs a "cold wall" process whereby a high energetic laser beam can be focused on a small spot at the surface of the target in the presence of high-purity gas. As of this writing, PLA has been applied to synthesize nanoparticles of metals,[13] semiconductors,[14] and ceramics.[15] In recent efforts to overcome the problem of controllability, several groups have applied a differential mobility analyzer (DMA)[16,17,18] to the PLA system. However, these investigations were limited to single-component or uniformly structured nanoparticles.

The combination of multicomponent material is thought to hold promise as a method not only for isolating nanosize domains but also for obtaining novel properties via the exchange interaction. When nanoparticles are fabricated from magnetic materials, the interaction between magnetically soft and hard substances is expected to generate magnetic exchange-coupling.[19] In recent experiments to utilize the exchange-coupling between FePt and Fe_3Pt, Zeng et al.[20] obtained an energy product of 50%, exceeding the theoretical limit of FePt. The use of simple elements such as ferromagnetic Ni and antiferromagnetic NiO[21] might also produce a similar effect.

In this study, we employed a combination of PLA and DMA with postannealing and compulsory oxidation to fabricate an isolated Ni core with an NiO shell structure using a newly proposed gas-phase sequential process and method for individual control.

* To whom correspondence should be addressed. E-mail: t.seto@aist.go.jp.
† Also at the Research Center for Advanced Manufacturing on Nanoscale Science and Engineering, National Institute of Advanced Industrial Science and Technology (AIST), AIST East, 1-2-1 Namiki, Tsukuba 305-8564, Japan.
‡ Also at the Nanotechnology Research Institute, National Institute of Advanced Industrial Science and Technology (AIST), AIST Central 5, 1-1-1 Higashi, Tsukuba 305-8565, Japan.
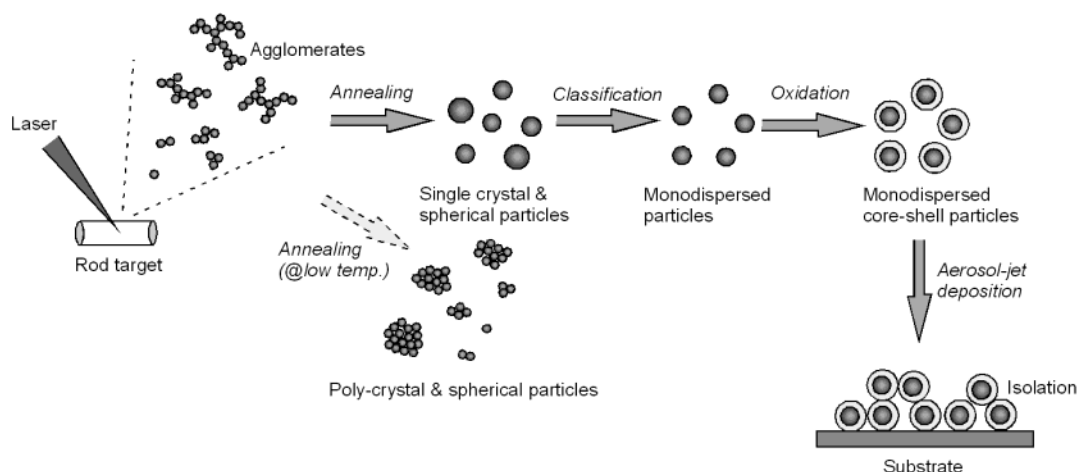
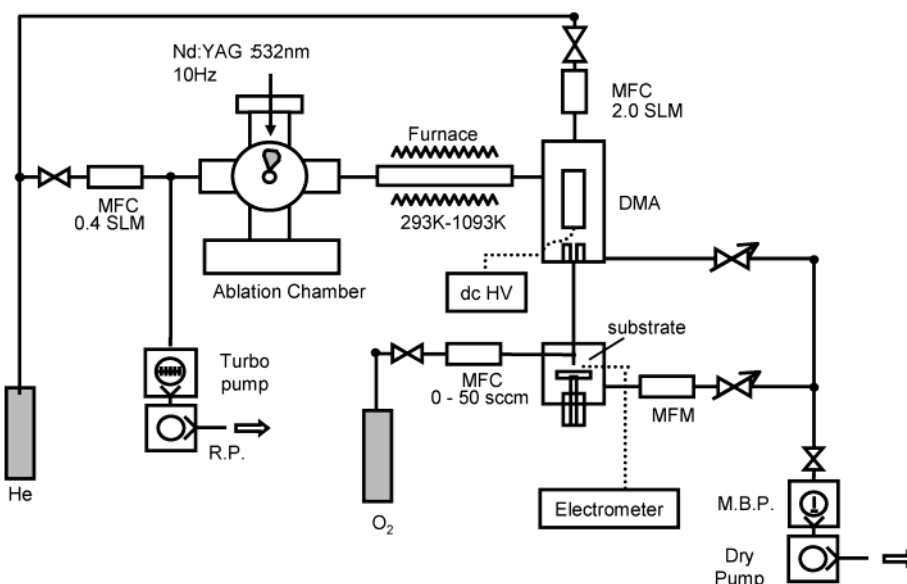**Figure 1.** Schematic illustration of the gas-phase sequential process.

Figure 2. Experimental system used in this study.

Experimental Section

A. Basic Concept. All processes and strategies proposed in this study are schematically illustrated in Figure 1. Our challenge was to develop a fundamental technology to fabricate nanometer order heterostructures (i.e. Ni/NiO core shell structures) with controlled impurity, crystal phase, size, and surface structure using a gas-phase process compatible with semiconductor processing. To accomplish this task, we employed a method of "laser nanoprototyping" in the following steps:

(i) preparation of nanoparticles by pulsed laser ablation (PLA);

(ii) control of crystallinity by aerosol postannealing;

(iii) size control by differential mobility analyzer (DMA);

(iv) modification of surface structure by compulsory oxidation;

(v) deposition by aerosol jet.

Steps i to iv are all operated in the sequential gas stream, and each takes place in less than 1 s. Though applicable to a variety of metal/metal oxide systems, it was applied here on a trial basis to control the size of the nanosized ferromagnetic domain (i.e. Ni particle diameter) and isolate the nanoparticles with antiferromagnetic shells (i.e. NiO). The entire experimental setup is shown in Figure 2. The system consists of mainly five parts: a laser ablation chamber; a furnace for aerosol postan-

nealing; a DMA; a coaxial cylindrical nozzle for compulsory oxidation; a deposition chamber.

B. Nanoparticle Preparation by PLA. In the ablation part, a second harmonic pulsed Nd:YAG laser (wavelength, 532 nm; power, 130−140 mJ/pulse; pulse width, about 5 ns) was focused by a single lens on a nickel rod (i.d. 10 mm) rotating at 20 rounds/min to produce high-purity Ni particles. The chamber was evacuated to a pressure below 10^{-4} Pa before the experiments. Helium was introduced as background gas, at a constant flow rate of 0.4 SLM (standard liters per minute) controlled by a mass flow controller (MFC). The pressure of the ablation chamber was kept at 1 kPa using variable conductance valves.

C. Control of Crystallinity by Postannealing. The particles were fed out from the laser ablation chamber through a quartz tube (i.d., 12.5 mm; length, 0.6 m) into the annealing furnace, a single-stage tubular heater with a gold infrared reflector. A constant temperature zone was generated over the length of 0.2 m. The furnace temperature was adjusted within a range from 293 K (room temperature) to 1073 K to investigate morphological changes due to crystallization within the furnace.

D. Classification of Nanoparticle by DMA. The first DMA was developed by Knutson and Whitby[22] in 1975 for the measurement of atmospheric aerosol, and later studies demonstrated the performance of the classification system and
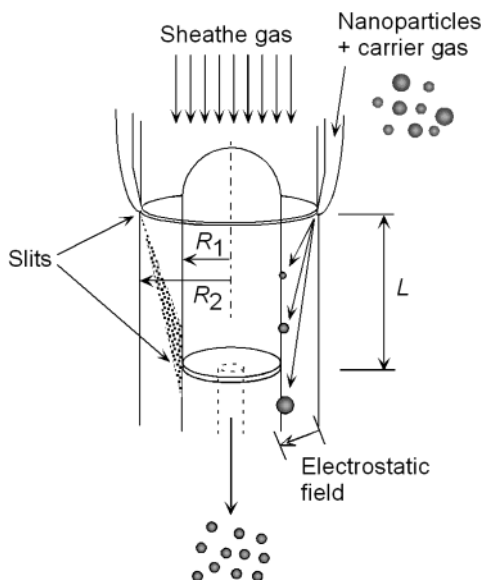
Size-Selected Ni/NiO Core−Shell Particles

J. Phys. Chem. B, Vol. 108, No. 2, 2004 **525**

Figure 3. Schematic illustration of DMA.

discussed its finer points.[23−26] We employed the Vienna-type DMA[24] which was developed to classify the particles with the size range from 1 to 1000 nm. Our LP-DMA system is specially tuned to classify the nanoparticles less than 20 nm where their properties might change drastically due to the size reduction. The minimum diameter of nanoparticles which we have been observed was about 3 nm because of significant particle loss during transport and low production yield due to very low charging efficiency.

We placed [241]Am at the inlet of the DMA to charge the nanoparticles in the helium gas stream by having them collide with ions generated by α-ray irradiation. The particles within the DMA were differentially classified utilizing the balance of electrical mobility and helium gas flow. Figure 3 shows a cross-sectional illustration of the low-pressure differential mobility analyzer (LP-DMA; Wycoff Co. Ltd.) used in this study. A dry pump with a mechanical booster pump was used to maintain a pressure of 1000 Pa during operation.

Knutson and Whitby[22] gave the median value of the electrical mobility of the classified particles as a function of the applied voltage, V, the sheath gas flow rate, Q_c, and the three dimensions of the DMA, L, R_1, and R_2 (shown in Figure 3).

$$Z_{PC} = Q_c \frac{\ln(R_2/R_1)}{2\pi LV}$$

The gas flow rate (Q_c) in this study was 2.0 SLM, and the dimensions of the DMA were $L = 16$ mm, $R_1 = 25$ mm, and $R_2 = 33$ mm. The electrical mobility was also related to the particle diameter, d_p, as

$$Z_P = \frac{qe\left[1 + \frac{\sqrt{2}kT}{\pi\sigma^2 pd_p}\left(1.257 + 0.40 \exp\left(\frac{-0.778\pi\sigma^2 pd_p}{kT}\right)\right)\right]}{3\pi\mu d_p}$$

where q, e, μ, k, T, σ, and p are the number of elementary electrical charges, the elementary electrical charge, the viscosity of gas, the Boltzmann constant, the temperature, the collision parameter of a gas molecule, and the pressure, respectively. We obtain the DMA voltage (V) corresponding to the desirable particle diameter by the above two equations. These values are listed in Table 1.
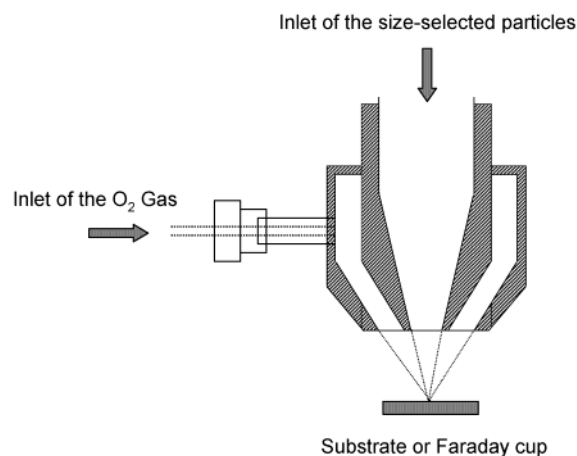

Figure 4. Cross-sectional view of compulsory oxidation nozzle for aerosol-jet deposition.

TABLE 1: Relationship between DMA Applied Voltage, V, and Particle Diameter, d_p

	V (V)			
	5.84	23.4	52.6	93.6
d_p (nm)	5	10	15	20

The throughput (=obtained particles/generated particles) of our system is not high due to the significant loss and low charging efficiency of nanoparticles (the order of 0.1−0.01%[26]) as mentioned before. On the other hand, the mass production rate is reasonable (the order of 1 μg/h) for analyzing their size-dependent properties, because we can synthesize highly concentrated nanoparticles by pulsed laser ablation.

E. Compulsory Oxidation and Deposition Process. Compulsory rapid oxidation of the particles and deposition were carried out simultaneously in the deposition chamber. The oxidation nozzle is schematically illustrated in Figure 4. The nozzle consists of a series of coaxial cylindrical tubes, the outermost of which is connected to the oxygen line. Oxygen was introduced from the outer tube and then mixed with the helium and size-selected particle gas stream before the deposition. For the observation of size, morphology, and surface structure of the generated nanoparticles by a transmission electron microscope (TEM), the particles were deposited on a TEM microgrid. The microgrid was transferred to a high-resolution electron microscope (JEOL JEM-2010, acceleration voltage = 200 kV, $\lambda = 0.002\,509$ nm) with an LaB$_6$ filament. We also performed an electron diffraction pattern analysis.

An in situ measurement of the number density of the gas-phase particles (C) from their current (I) by the electrometer (EM) produced the value

$$C = I/(qeQ_a)$$

where q is number of charges (about unity), e is the elemental charge (=1.6 × 10^{-19}), and Q_a is the aerosol flow rate (=0.4 SLM). The size distribution of gas-phase particles can be obtained by scanning the DMA applied voltage and measuring the number density.

Results and Discussion

A. Improvement of Morphology by Aerosol Postannealing. Figure 5a−f shows transmission electron micrographs of particles with a mobility equivalent diameter of 10 nm according to DMA classification. Figure 5a,d shows the particles generated by laser ablation without annealing (i.e., at room temperature,
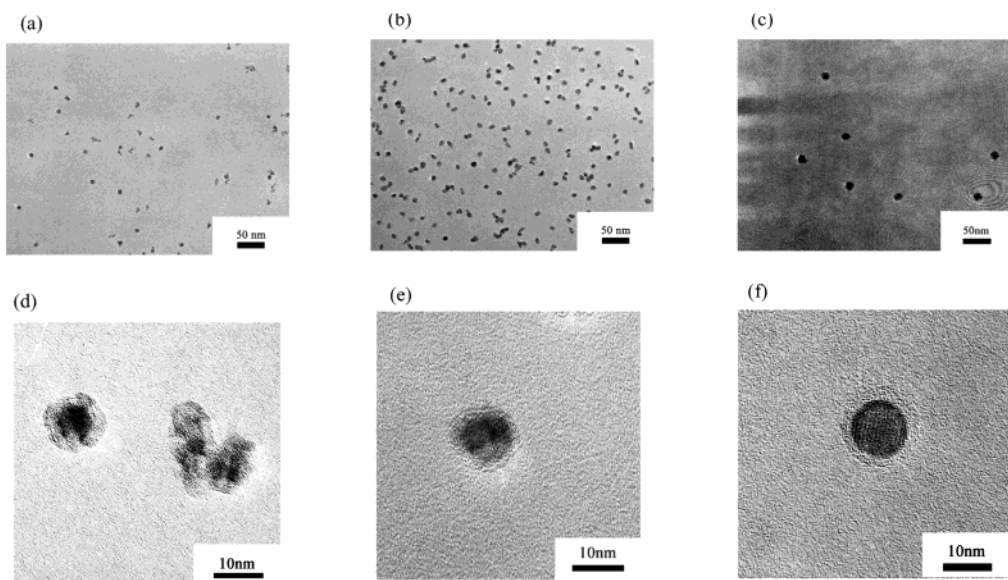
Figure 5. Transmission electron micrographs of particles with a mobility equivalent diameter of 10 nm according to DMA classification. The particles were annealed at (a) 293, (b) 673, and (c) 1073 K, respectively. (d)−(f) show high-resolution TEM images corresponding to (a)−(c).

293 K) and without compulsory oxidation. The particles before annealing exhibited agglomerated structures due to Brownian coagulation between the smaller particles in the gas phase. These agglomerates were composed of primary particles of about 4 nm in diameter. The high-magnification image in Figure 5d shows the presence of some spherical particles among the large population of agglomerates. When the furnace temperature was increased to 673 K (Figure 5b,e) and 1073 K (Figure 5c,f), the agglomerates were sintered into spheres within the furnace. The surfaces of these annealed particles were partially covered by an amorphous layer, a probable result of the chemical reaction with room air or with the carbon microgrid during transport to the TEM. As shown in Figure 5b,c, no agglomerates were observed at the diameter of 10 nm and at the temperatures of 673 and 1073 K. From the high-magnification TEM images (typically shown in Figure 5e,f), the mean thickness of surface amorphous layer was estimated to be about 0.5 nm, as mentioned later. Figure 5e indicates that the particles were spherical but polycrystalline and clearly in need of further annealing to acquire a single-crystal structure. Most of the Ni nanoparticles were single crystals after 1073 K annealing, as shown in Figure 5f. Accordingly, we used furnace temperature of 1073 K for further experiments. Before discussing the effect of particle size, we will demonstrate a simple calculation on the morphological change due to sintering.

The sintering characteristic time, τ, is defined as the time that the doublet (a pair of coagulated particles with the same diameters) can be sintered into a single sphere.[27] The sintering characteristic time of a Ni nanoparticle based on the grain boundary diffusion model is presented as

$$t = 6.54 \times 10^{19} T d_p^4 \exp(1.08 \times 10^5/RT)$$

where T is the temperature, R is the gas constant, and d_p is the primary particle diameter. The grain boundary diffusion coefficient, an activation energy, and other physical properties were obtained from ref 28. Figure 6 shows the change in τ with the primary particle diameters at the temperatures 273, 673, and 1073 K. In the present experimental conditions (pressure, 1000 Pa; flow rate, 0.4 SLM; heating tube i.d., 12.5 mm; effective heating length, 0.2 m), the residence time, t_r, is 0.147 s for 273
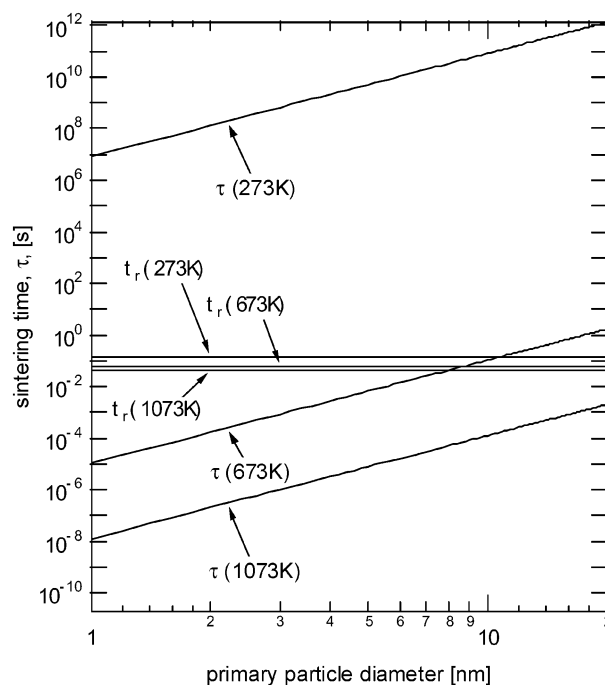

Figure 6. Sintering characteristic time for Ni nanoparticles.

K, 0.06 s for 673 K, and 0.04 s for 1073 K, respectively, as plotted in Figure 6.

Figure 6 shows that particles with diameter of 8 nm can be sintered into a single sphere at a temperature of 673 K, as indicated by the point at which $\tau(d_p) = t_r$. The temperature 1073 K is clearly sufficient to obtain a single spherical particle with a diameter of 20 nm. As described later, we experimentally observed some spherical but polycrystal particles with 20 nm in diameter even in the case of 1073 K postannealing. This was probably because some of the initial agglomerates had a complex fractal-like shape and because the time required for recrystallization might have exceeded the sintering time. However, we could obtain single-crystal particles with diameters of 15, 10, and 5 nm after the 1073 K annealing.

Figure 7 shows the number density curve against corresponding DMA applied voltages (size distributions) of the gas-phase particles with annealing (673 and 1073 K) and without anneal-
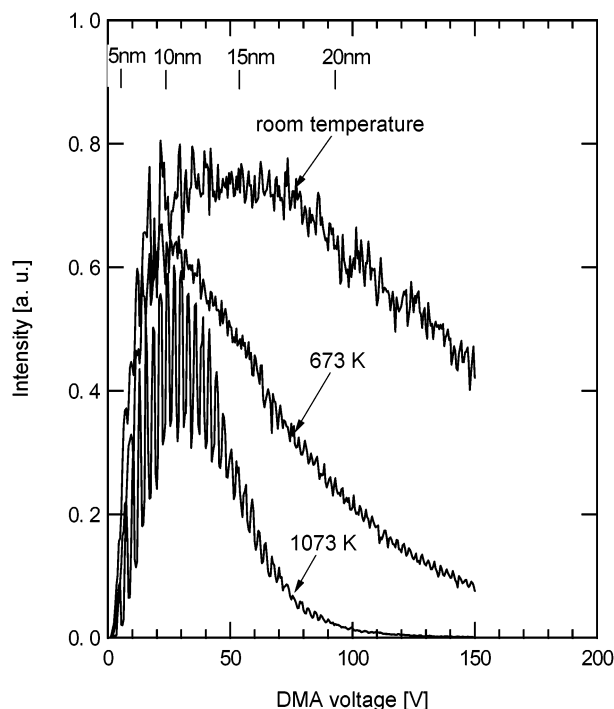
Size-Selected Ni/NiO Core−Shell Particles

J. Phys. Chem. B, Vol. 108, No. 2, 2004 **527**

Figure 7. Number densities against corresponding DMA applied voltage.

ing, obtained by DMA and an electrometer (EM). The peak diameter without annealing was about 15 nm ($V = 50$ V), and the distribution curve has a tail indicating a significant presence of the larger particles. The geometric mean diameter and standard deviation of generated particles before classification were 15 nm and 1.5 for the room temperature and 10 nm and 1.3 for annealed at 1073 K, respectively. The annealing resulted in a clear reduction in the width of the peak due to the decrease in the mobility-equivalent diameter (proportional to the square root of the surface area of the particle) by the restructuring and sintering.

B. Size Selection of Ni Nanoparticles. Figure 8a−d shows typical TEM images of Ni nanoparticles of 5, 10, 15, and 20 nm in diameter annealed at 1073 K. No agglomerates were found in any of the cases, since the nanoparticles were annealed to single spheres to form monodispersed Ni particles, as discussed in the previous section. It should be noted that some of the 20 nm particles remained polycrystalline in structure.

Particle size distributions based on the projected area equivalent diameter of classified Ni particles were obtained using digital image analysis of 100−300 particles in the digitally scanned TEM images, as shown in Figure 9. The particles classified from 5 to 20 nm clearly exhibited very narrow band distributions. Geometric mean diameters were 4.81, 10.6, 14.92, and 20.74 nm when the DMA mobility-equivalent diameters were set at 5, 10, 15, and 20 nm, respectively. The mean diameter for the 20 nm particles were slightly larger than the value set for the DMA since some of the particles were polycrystalline and had a surface roughness that might have increased the particle mobility. Geometric standard deviations were 1.09, 1.19, 1.09, and 1.13 for 5, 10, 15, and 20 nm, respectively. These results show that the DMA was effective at producing monodispersed nanoparticles. As shown in Figures 8, the particles without compulsory oxidation had no surface oxidized layer (Figure 8c) or coated with various thickness of the amorphous oxide layer (Figure 8a,b,d; also Figure 5f). They are considered to be oxidized during the transport from a vacuum chamber to a TEM. The average thickness of surface
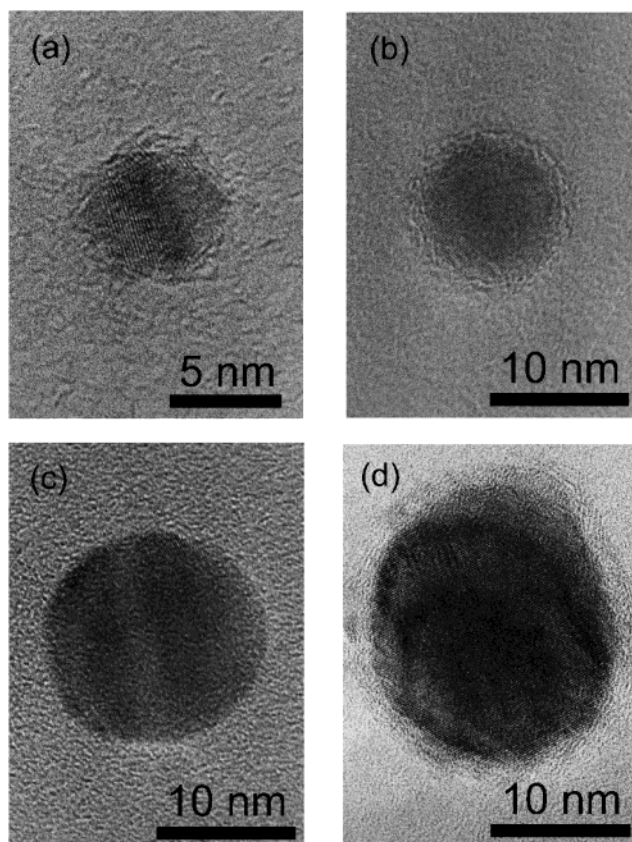

Figure 8. High-resolution TEM images of Ni nanoparticles classified by DMA to be (a) 5, (b) 10, (c) 15, and (d) 20 nm, respectively.

oxidized layer before compulsory oxidation was 0.5 nm. The next section we will summarize our evaluation of the thicknesses of the oxidized layers.

C. Fabrication of Core−Shell Structure. To isolate each individual particle as it was being deposited on the substrate, we employed compulsory oxidation after the LP-DMA and before the landing onto the substrate. Figure 9a−h shows TEM images of the particles isolated by compulsory oxidation. The high-magnification images clearly revealed the edges and crystalline structures of the oxidized shell after the compulsory oxidation (Figure 9e−h), in marked contrast to the images of the particles formed without oxidation (Figures 8). Rellinghaus et al.[29] obtained structures similar to those shown in Figures 8 (Ni core with amorphous shell) after subsequent oxidation in ambient air. They also observed the recrystallization of the NiO shell during electron beam irradiation in a TEM. In our case, clear difference between compulsory oxidation and subsequent oxidation was seen in the electron diffraction (ED) patterns of 10 nm particles (Figure 10). Though it was difficult to obtain the electron diffraction from 5 nm particles, the diffraction from 15 and 20 nm particles exhibited lines similar to those of the 10 nm particles. The lattice parameters (d_{100}) used for the assignment of ED patterns were 0.3524 nm for fcc Ni and 0.4168 nm for rhombohedoral NiO. Strong lines from (111), (200), (220), (311), (222), and (420) of Ni were observed for the particles formed without oxidation (Figure 10a). The compulsorily oxidized particles exhibited the same lines as those shown in Figure 10a, as well as some strong lines from the crystal structures of NiO (Figure 10b). It should be noted that no lines from $Ni(OH)_2$ were recognized in Figure 10a,b. These results clearly indicate that the mixing of oxygen with Ni particles was effective not only for the formation of the oxide shell but also for the crystallization of the NiO.
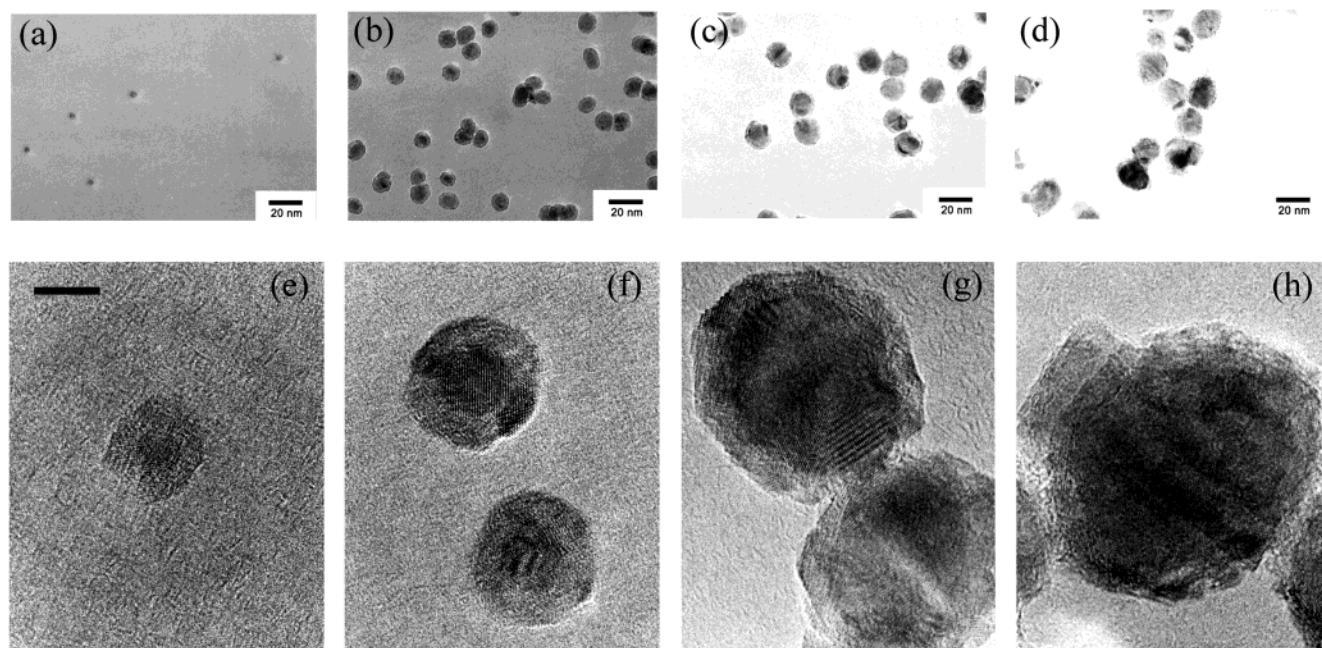
Figure 9. Transmission electron micrographs of Ni/NiO particles isolated by compulsory oxidation with the mobility equivalent diameters of (a) 5 nm, (b) 10 nm, (c) 15 nm, and (d) 20 nm, respectively. (e)−(h) are high-magnification images corresponding to (a)−(d). The size bar for (e)−(h) is 5 nm.
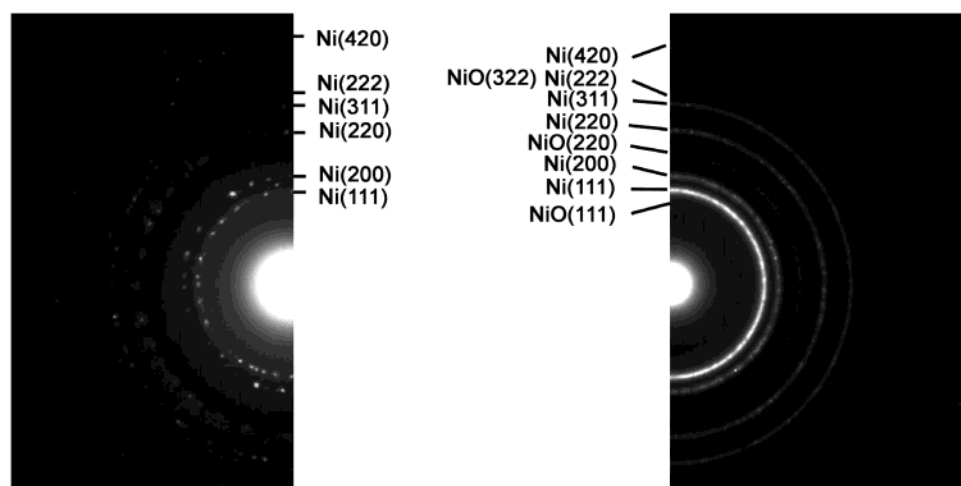

Figure 10. Electron diffraction of Ni nanoparticles (a) without and (b) with compulsory oxidation.

TABLE 2: Mean Thickness of Surface Oxide Layer without/ with Compulsory Oxidation

	DMA setting diameter (nm)	
	10	15
without (nm)	0.50	0.52
with (nm)	2.03	1.99

Table 2 lists the mean thicknesses of the shells (NiO) with annealing and without annealing. The oxide layer can be grown by compulsory oxidation from 0.5 to 2 nm regardless of the particle diameter (10 and 15 nm). These results suggest that the chemical reaction between Ni and oxygen proceeded at the surface of the Ni nanoparticles and might have had enough energy to crystallize the shell. The shell with the 2 nm thickness protected the Ni core from further oxidation. The oxidized layer might have also protected the particles from subsequent oxidations by chemical reactions with room air or moisture encountered during transportation.[30] The formation of the crystalline NiO shell isolates each individual Ni core since the surface coagulations and contact of the Ni with Ni can progress without

oxidation before landing on the substrate. The NiO shell is expected to be applicable not only for the isolation of the magnetic domain but also for the induction of the exchange-coupling. In future studies we may investigate the latter use.

Conclusions

A fundamental technique to fabricate monodispersed and nanosized Ni/NiO core−shell particles was performed through a combination of five gas-phase processes, namely, PLA, aerosol postannealing, DMA, compulsory oxidation, and aerosol jet deposition. Spherical Ni particles could be formed at the higher annealing temperatures. The 5, 10, and 15 nm diameter particles were single crystals, whereas the 20 nm particles included both single crystals and polycrystalline structures. Thus, it appears that heat treatment at much higher temperatures is required for 20 nm particles. The mean thicknesses of the shells were 0.5 nm without compulsory oxidation and 2 nm with the compulsory oxidation. The oxidized layer with compulsory oxidation showed a crystalline structure and clear edge. Our results on the

Size-Selected Ni/NiO Core−Shell Particles

J. Phys. Chem. B, Vol. 108, No. 2, 2004 **529**

fabrication of Ni/NiO particles isolated with controlled sizes and surface layers suggest that it may be possible to control their magnetic properties.

References and Notes

(1) Volokitin, Y.; Sinzig, J.; deJongh, L. J.; Schmid, G.; Vargaftik, M. N.; Moiseev, I. I. *Nature* **1996**, *384*, 621.

(2) Majetich, S. A.; Jin, Y. *Science* **1999**, *284*, 470.

(3) Neel, L. *Ann. Geophys. (CNRS)* **1949**, *5*, 99.

(4) Sun, S. H.; Murray, C. B.; Weller, D.; Folks, L.; Moser, A. *Science* **2000**, *287*, 1989.

(5) Woods, S. I.; Kirtley, J. R.; Sun, S. H.; Koch, R. H. *Phys. Rev. Lett.* **2001**, *87*, 137205.

(6) Sun, S. H.; Zeng, H. *J. Am. Chem. Soc.* **2002**, *124*, 8204.

(7) Yatsuya, S.; Uyeda, R. *Oyo Butsuri* **1973**, *42*, 1067−85.

(8) Okuyama, K.; Kousaka, Y.; Tohge, N.; Yamamoto, S.; Wu, J. J.; Flagan, R. C.; Seinfeld, J. H. *AIChE J.* **1986**, *32*, 2010.

(9) Ulrich, G. D. *Chem. Eng. News* **1984**, *62*, 22.

(10) Sun, X. C.; Dong, X. L. *Mater. Res. Bull.* **2002**, *37*, 991.

(11) Kuhn, L. T.; Bojesen, A.; Timmermann, L.; Nielsen, M. M.; Morup, S. *J. Phys: Condens. Mater.* **2002**, *14*, 13551.

(12) Chrisey, D. B., Hubler, G. K., Eds.; *Pulsed laser deposition of thin films*; Wiley-Interscience: New York, 1994.

(13) Jonsson, B. J.; Turkki, T.; Strom, V.; ElShall, M. S.; Rao, K. V. *J. Appl. Phys.* **1996**, *79*, 5063.

(14) Lowndes, D. H.; Rouleau, C. M.; Thundat, T. G.; Duscher, G.; Kenik, E. A.; Pennycook, S. J. *J. Mater. Res.* **1999**, *14*, 359.

(15) Ogawa, K.; Vogt, T.; Ullmann, M.; Johnson, S.; Friedlander, S. K. *J. Appl. Phys.* **2000**, *87*, 63.

(16) Camata, R. P.; Hirasawa, M.; Okuyama, K.; Takeuchi, K. *J. Aerosol Sci.* **2000**, *31*, 391.

(17) Suzuki, N.; Makino, T.; Yamada, Y.; Yoshida, T.; Seto, T. *Appl. Phys. Lett.* **2001**, *78*, 2043.

(18) Seto, T.; Kawakami, Y.; Suzuki, N.; Hirasawa, M.; Aya, N. *Nano Lett.* **2001**, *1*, 315.

(19) Kneller, E. F.; Hawig, R. *IEEE Trans. Magn.* **1991**, *27*, 3588.

(20) Zeng, H.; Li, J.; Liu, J. P.; Wang, Z. L.; Sun, S. *Nature* **2002**, *420*, 395.

(21) Sako, S.; Ohshima, K.; Sakai, M.; Bandow, S. *J. Vac. Sci. Technol.* **1997**, *B15*, 1338.

(22) Knutson, E. O.; Whitby, K. T. *J. Aerosol Sci.* **1975**, *6*, 443.

(23) Kousaka, Y.; Okuyama, K.; Adachi, M. *Aerosol Sci. Technol.* **1985**, *4*, 209.

(24) Reischl, G. P. *Aerosol Sci. Technol.* **1991**, *14*, 5.

(25) de Juan, L.; de la Mora, J. F. *J. Aerosol Sci.* **1998**, *29*, 617.

(26) Seto, T.; Nakamoto, T.; Okuyama, K.; Adachi, M.; Kuga, Y.; Takeuchi, K. *J. Aerosol Sci.* **1997**, *28*, 193.

(27) Kobata, A.; Kusakabe, K.; Morooka, S. *AIChE J.* **1991**, *37*, 347.

(28) German, R. M. *Powder Metallurgy Science*; Metal Powder Ind. Fed.: Princeton, NJ, 1984.

(29) Rellinghaus, B.; Stappert, S.; Wassermann, E. F.; Sauer, H.; Spliethoff, B. *Eur. Phys. J. D* **2001**, *16*, 249.

(30) Uchikoshi, T.; Sakka, Y.; Yoshitake, M.; Yoshihara, K. *NanoStruct. Mater.* **1994**, *4*, 199.